

# Infrared dielectric properties of low-stress silicon nitride

Giuseppe Cataldo,<sup>1,2,\*</sup> James A. Beall,<sup>3</sup> Hsiao-Mei Cho,<sup>3</sup>  
Brendan McAndrew,<sup>1</sup> Michael D. Niemack,<sup>3</sup> and Edward J. Wollack<sup>1</sup>

<sup>1</sup>NASA Goddard Space Flight Center, 8800 Greenbelt Road, Greenbelt, MD 20771, USA

<sup>2</sup>Universities Space Research Association, 10211 Wincopin Circle, Columbia, MD 21044, USA

<sup>3</sup>National Institute of Standard and Technology, 325 Broadway, Boulder, CO 80305, USA

\*Corresponding author: Giuseppe.Cataldo@nasa.gov

Compiled February 21, 2022

Silicon nitride thin films play an important role in the realization of sensors, filters, and high-performance circuits. Estimates of the dielectric function in the far- and mid-infrared regime are derived from the observed transmittance spectra for a commonly employed low-stress silicon nitride formulation. The experimental, modeling, and numerical methods used to extract the dielectric parameters with an accuracy of approximately 4% are presented. © 2022 Optical Society of America

OCIS codes: 310.3840, 310.6188, 310.6860.

The physical properties of silicon nitride thin films, namely low tensile stress, low thermal/electrical conductance, and its overall compatibility with other common materials, have facilitated its use in the micro-fabrication of structures requiring mechanical support, thermal isolation, and low-loss microwave signal propagation (e.g., [1–4]). Silicon nitride films are amorphous, highly absorbing in the mid-infrared [5], and their general properties are functions of composition [6, 7]. Here, the optical properties are studied in detail for a membrane with parameters commonly employed in micro-fabrication.

The silicon nitride optical test films were prepared by a LP-CVD (Low-Pressure Chemical-Vapor-Deposition) process optimized for low tensile stress and refractive index [8]. The 5:1 SiH<sub>2</sub>Cl<sub>2</sub>/NH<sub>3</sub> gas ratio employed results in a tensile stress < 100 MPa and optical index greater than ~ 2 [9]. The test structure is shown schematically in Fig. 1 (inset). Double-side-polished silicon (75-mm-diameter, 500-μm-thick) wafers [10] were used as a mechanically robust handling structure for the SiN<sub>x</sub> membranes. A 150-nm thermal oxide was grown on the silicon wafers by wet oxidation at 950°C for 31 minutes. This layer was subsequently used as an etch stop to protect the nitride during definition of the silicon handling wafer geometry. A low-stress SiN<sub>x</sub> layer was then deposited by LP-CVD (e.g., deposition parameters for 2-μm film are 835°C for 9.7 hours with pressure 33 Pa and 12 sccm NH<sub>3</sub>, 59 sccm SiH<sub>2</sub>Cl<sub>2</sub>). The wafers were then patterned with a resist mask and SiN<sub>x</sub>/SiO<sub>2</sub> windows formed by deep reactive ion etching which removed all the silicon under the window area. The residual thermal oxide was removed with HF vapor etch leaving a set of uniform SiN<sub>x</sub> membranes each with a 10-mm diameter aperture individually suspended from the silicon handling frame.

The optical tests were performed on SiN<sub>x</sub> samples having membrane thicknesses of 0.5 and 2.3 μm with a uncertainty of 3%. Fabry-Perot resonators were made by stacking multiple samples with silicon standoff frames between adjacent samples to explore the long-wavelength response of the material in greater detail. The silicon standoffs allowed a vent path for evacuation of air be-

tween the nitride membranes. All optical measurements were performed in vacuum with a residual pressure less than 100 Pa.

The samples were characterized with a Bruker 125 high-resolution Fourier Transform Spectrometer (FTS) and were measured in transmission at the focal plane of an *f*/6 beam. A number of different sources, beam splitters, and detector configurations were used in combination to provide measurements over the reported spectral range. The single-layer SiN<sub>x</sub> sample transmission was measured over an extended range from 15 to 10000 cm<sup>-1</sup>. The mercury lamp and a multilayer Mylar beam splitter were used to access frequencies below 600 cm<sup>-1</sup>. Additional mid-infrared spectral data up to 2400 cm<sup>-1</sup> were acquired using a ceramic glow bar source, Ge-coated KBr beam splitter, and room-temperature DTGS detector. The remaining near-infrared data up to 10000 cm<sup>-1</sup> were taken with a W filament source, Si on CaF<sub>2</sub> beam splitter, and a liquid-nitrogen-cooled InSb detector (Fig. 1). Far-infrared data between 15 and 95 cm<sup>-1</sup> were taken using a mercury arc lamp source and a liquid-helium-cooled 4.2-K bolometer. Mylar beam splitters of 50-, 75- and 125-μm thicknesses and a multilayer Mylar beam splitter were used during separate scans (Fig. 2). The resultant transmission data were merged into a single spectra using a signal-to-noise weighting for subsequent parameter extraction.

The dielectric response is represented as a function of frequency,  $\omega$ , by the classical Maxwell-Helmholtz-Drude dispersion model [11]:

$$\hat{\epsilon}_r(\omega) = \hat{\epsilon}_\infty + \sum_{j=1}^M \frac{\Delta\hat{\epsilon}_j \cdot \omega_{Tj}^2}{\omega_{Tj}^2 - \omega^2 - i\omega\Gamma'_j(\omega)} \quad (1)$$

where  $M$  is the number of oscillators and  $\hat{\epsilon}_r = \epsilon'_r + i\epsilon''_r$  is a complex function of  $(5M+2)$  degrees of freedom, which are as follows: the contribution to the relative permittivity  $\hat{\epsilon}_\infty = \hat{\epsilon}_{M+1}$  of higher lying transitions, the difference in relative complex dielectric constant between adjacent oscillators  $\Delta\hat{\epsilon}_j = \hat{\epsilon}_j - \hat{\epsilon}_{j+1}$  which serves as a measure of the oscillator strength, the oscillator resonance frequency

$\omega_{T_j}$ , and the effective Lorentzian damping coefficient  $\Gamma'_j$ , for  $j = 1, \dots, M$ . The following functional form is used to specify the damping:

$$\Gamma'_j(\omega) = \Gamma_j \exp \left[ -\alpha_j \left( \frac{\omega_{T_j}^2 - \omega^2}{\omega \Gamma_j} \right)^2 \right] \quad (2)$$

where  $\alpha_j$  allows interpolation between Lorentzian ( $\alpha_j = 0$ ) and Gaussian wings ( $\alpha_j > 0$ ) similar to the approach in [12]. The form indicated above enables a more accurate representation of relatively strong oscillator features.

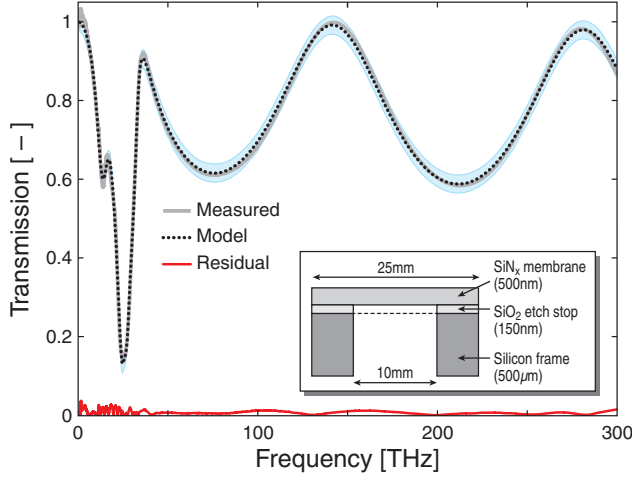


Fig. 1. (Color online) Room-temperature transmission of a silicon nitride sample  $0.5 \mu\text{m}$  thick: measured (grey), model (black dotted), and residual (red). The shaded band's width delimits the estimated  $3\sigma$  measurement uncertainty. A 30 GHz ( $1 \text{ cm}^{-1}$ ) resolution is employed for the measurement. The insert depicts the geometry of the  $\text{SiN}_x$  membrane and micro-machined silicon frame.

The impedance contrast between free space and the thin-film sample forms a Fabry-Perot resonator. The observed transmission can be modeled [13] as a function of the dielectric response (Eq. 1), thickness, and wavenumber. The dielectric parameters were solved by means of a non-linear least-squares fit of the transmission equation to the laboratory FTS data. Specifically, a sequential quadratic programming (SQP) method with computation of the Jacobian and Hessian matrices [14, 15] was implemented. The merit function,  $\chi^2$ , was used in a constrained minimization over frequency as follows:

$$\min_{\text{DOF}} \chi^2 = \min_{\text{DOF}} \sum_{k=1}^N \left[ T(\hat{\epsilon}_r(\omega), h) - T_{\text{FTS}_k} \right]^2 \quad (3)$$

where  $N$  is the number of data points,  $T$  the modeled transmittance,  $T_{\text{FTS}}$  the measured transmittance data, and  $h$  is the measured sample thickness. We are guided by the Kramers-Kronig relations in defining constraints for a passive material:  $|\hat{\epsilon}_j| > |\hat{\epsilon}_{j+1}|$ ,  $\epsilon''_j > 0$  and  $\hat{\epsilon}_r(0) = \hat{\epsilon}_1$  [16]. For accurate parameter determination the sample should have uniform thickness, be

adequately transparent to achieve high signal-to-noise, and have diffuse scattering as a sub-dominate process. The method requires an *a posteriori* numerical verification for Kramers-Kronig consistency. In the example presented here, a numerical Hilbert transform [17] of  $\epsilon''_r(\omega)$  reproduces  $\epsilon'_r(\omega)$  to within 2% (Fig. 3). An alternative method employing reflectivity and phase allows *a priori* Kramers-Kronig consistent results [18]. However, given the details of the thin-film samples and available instrumentation, this approach was not implemented.

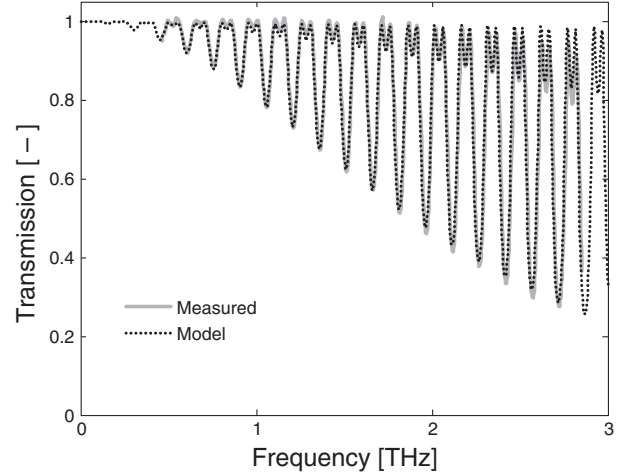


Fig. 2. (Color online) Measured (solid grey) and model (black dotted) transmission for a 3-layer stack of silicon nitride samples  $2.3 \mu\text{m}$  in thickness with  $998\text{-}\mu\text{m}$  inter-membrane delays which complements the data shown in Fig. 1. The sample response in the far-infrared was acquired with a resolution of 3 GHz ( $0.1 \text{ cm}^{-1}$ ).

Figure 1 illustrates the measured and modeled results obtained from the analysis of a  $0.5\text{-}\mu\text{m}$ -thick sample. The peak residual in the transmittance is less than 3% and the  $3\sigma = 0.023$  uncertainty band indicated corresponds to the 99.7% confidence level. The standard deviation adopted for the measured data,  $\sigma$ , was estimated assuming the errors as a function of frequency are uniform and have a reduced  $\chi^2$  equal to unity. An additional uncertainty in the FTS normalization influences the dielectric response function at the 1% level. In addition to the channel spectra, the observed spectrum shows two predominant features at 12 THz and 25 THz. Simulations with  $M = 2$  oscillators lead to a peak residual on transmission of 5% and do not enable recovery of the resonance at 25 THz. Using 5 oscillators satisfactorily recovers the observed transmittance and reduces the peak residual by a factor of 4.4. When the resonator's quality factor,  $Q_{\text{eff}_j} = \omega_j / \Gamma'_j$ , is greater than 5, the data were not reproducible by either a pure Lorentzian oscillator or Eq. (4.6) in [12]. In these regions, the peak transmission residuals were decreased by a factor  $\sim 2$  through the use of Eq. (2).

In Fig. 3 the values of the real and imaginary components of the dielectric function are illustrated as a function of frequency. The uncertainty in  $\epsilon_r$  was propagated

and computed as described in [19]. Table 1 contains a summary of the best fit parameters for 5 oscillators, which can be used to reproduce the data shown in Fig. 3.

Table 1. Fit parameter summary

$j$ [—]	$\varepsilon'_j$ [—]	$\varepsilon''_j$ [—]	$\omega_{Tj}/2\pi$ [THz]	$\Gamma_j/2\pi$ [THz]	$\alpha_j$ [—]
1	7.582	0	13.913	5.810	0.0001
2	6.754	0.3759	15.053	6.436	0.3427
3	6.601	0.0041	24.521	2.751	0.0006
4	5.430	0.1179	26.440	3.482	0.0002
5	4.601	0.2073	31.724	5.948	0.0080
6	4.562	0.0124			

In order to characterize the long-wavelength portion of the dielectric function, Fabry-Perot resonators were realized from 1-, 2-, and 3-layer samples. Representative data for the 3-layer resonator stack is presented in Fig. 2. A multilayer transfer matrix analysis [13] is used to extract the dielectric function using the measured  $\text{SiN}_x$  (2.3  $\mu\text{m}$ ) and silicon spacer (998  $\mu\text{m}$ ) thicknesses. The circular symbols at 1.5 THz and 2.5 THz indicated in Fig. 3 were computed from a composite analysis of the 3 Fabry-Perot measurement sets. The horizontal range indicates the data used in each fit. The best estimates are  $\hat{\varepsilon}_r \approx 7.6 + i0.08$  over the range 2-3 THz and  $\hat{\varepsilon}_r \approx 7.6 + i0.04$  over 0.4-2 THz. The real component of the static dielectric function derived from the data is in agreement with prior reported parameters for this stoichiometry [4]. As shown in Fig. 3, the measurements are internally consistent and represent roughly a factor-of-three reduction in uncertainty relative to prior infrared  $\text{SiN}_x$  measurements identified by the authors [5–7]. The dielectric parameters reported here are representative of low-stress  $\text{SiN}_x$  membranes encountered in our fabrication and test efforts.

## References

- D. J. Goldie, A. V. Velichko, D. M. Glowacka, and S. Withington, *Appl. Phys.* **109**, 084507 (2011).
- G. Wang, V. Yefremenko, V. Novosad, A. Datesman, J. Pearson, R. Divan, C. L. Chang, L. Bleem, A. T. Crites, J. Mehl, T. Natoli, J. McMahon, J. Sayre, J. Ruhl, S. S. Meyer, and J. E. Carlstrom, *IEEE Trans. Appl. Superconductivity* **21** (3), 232–235 (2011).
- J. M. Martinis, K. B. Cooper, R. McDermott, M. Steffen, M. Ansmann, K. D. Osborn, K. Cicak, S. Oh, D. P. Pappas, R. W. Simmonds, and C. C. Yu, *Phys. Rev. Lett.* **95** (21), 210503 (2005).
- H. Paik and K. D. Osborn, *Appl. Phys. Lett.* **96** (7), 072505 (2010).
- T. Eriksson, S. Jiang, and C. Granqvist, *Appl. Opt.* **24**, 745–746 (1985).
- E. A. Taft, *J. Electrochem. Soc.* **118**, 1341–1346 (1971).
- E. D. Palik, *Handbook of Optical Constants of Solids*, Vol. 1 (Elsevier, 1998), pp. 771–774.
- M. Sekimoto, H. Yoshihara, and T. Ohkubo, *J. Vac. Sci. Technol.* **21** (4), 1017–1021 (1982).

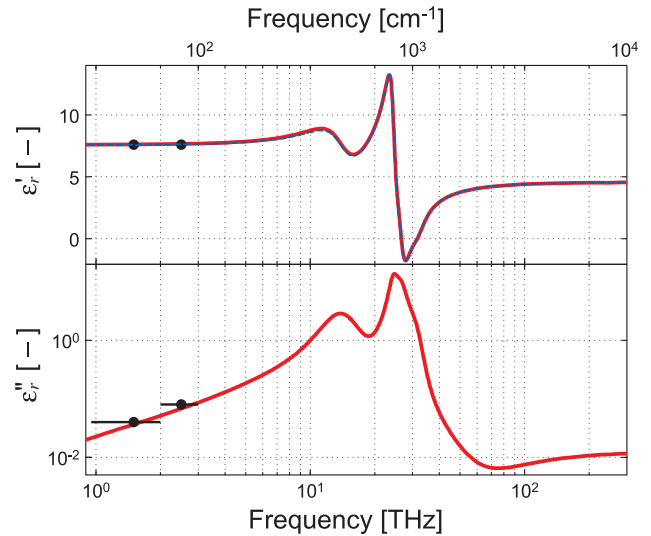


Fig. 3. (Color online) Real and imaginary parts (solid red lines) of the dielectric function as extracted from the data shown in Fig. 1. The line thickness is indicative of the propagated  $\sim 4\%$  error band. The numerical Hilbert transform of the modeled  $\varepsilon'_r(\omega)$  is indicated in the upper panel (dashed blue line) to facilitate comparison with  $\varepsilon'_r(\omega)$ . The filled symbols indicate the parameters derived from the data presented in Fig. 2.

- T. Makino, *J. Electrochem. Soc.* **130** (2), 450–455 (1983).
- Addison Engineering, 150 Nortech Parkway, San Jose, CA 95134. (Orientation  $\langle 100 \rangle$ , Czochralski, p-type B doped, bulk resistivity  $< 0.005 \Omega\text{-cm}$ )
- F. Gervais, “High-Temperature Infrared Reflectivity Spectroscopy by Scanning Interferometry” in *Electromagnetic Waves in Matter*, Part I, Vol. 8 (Infrared and Millimeter Waves), K. J. Button, eds. (Academic Press, London, 1983), pp. 284–287.
- C. C. Kim, J. W. Garland, H. Abad, and P. M. Raccach, *Phys. Rev. B* **45** (20), 11749 (1992).
- P. Yeh, *Optical Waves in Layered Media* (Wiley, New York, 1988), pp. 102–111.
- M. C. Biggs, “Constrained Minimization Using Recursive Quadratic Programming,” in *Towards Global Optimization*, L. C. W. Dixon and G. P. Szergo, eds. (North-Holland, 1975), pp. 341–349.
- M. J. D. Powell, “Variable Metric Methods for Constrained Optimization,” in *Mathematical Programming: The State of the Art*, A. Bachem, M. Grottschel and B. Korte, eds. (Springer Verlag, 1983), pp. 288–311.
- L. D. Landau and E. M. Lifshitz, *Electrodynamics of Continuous Media*, Vol. 8 (Pergamon Press, 1960), pp. 253–262.
- M. Mori and T. Ooura, “Double Exponential Formulas for Fourier Type Integrals with a Divergent Integrand,” in *Applicable Analysis*, Vol. 2 (World Scientific Series, 1993), pp. 301–308.
- R. Nitsche and T. Fritz, *Phys. Rev. B* **70** (19), 195432 (2004).
- W. H. Press, S. A. Teukolsky, W. T. Vetterling, and B. P. Flannery, *Numerical Recipes - The Art of Scientific Computing* (Cambridge University Press, 2007), pp. 799–806.

## Informational Fourth Page

In this section, please provide full versions of citations to assist reviewers and editors (OL publishes a short form of citations) or any other information that would aid the peer-review process.

## References

1. D. J. Goldie, A. V. Velichko, D. M. Glowacka, and S. Withington, "Ultra-low-noise MoCu transition edge sensors for space applications," *Appl. Phys.* **109**, 084507 (2011).
2. G. Wang, V. Yefremenko, V. Novosad, A. Datesman, J. Pearson, R. Divan, C. L. Chang, L. Bleem, A. T. Crites, J. Mehl, T. Natoli, J. McMahon, J. Sayre, J. Ruhl, S. S. Meyer, and J. E. Carlstrom, "Thermal Properties of Silicon Nitride Beams Below One Kelvin," *IEEE Trans. Appl. Superconductivity* **21** (3), 232–235 (2011).
3. J. M. Martinis, K. B. Cooper, R. McDermott, M. Steffen, M. Ansmann, K. D. Osborn, K. Cicak, S. Oh, D. P. Pappas, R. W. Simmonds, and C. C. Yu, "Decoherence in Josephson Qubits from Dielectric Loss", *Phys. Rev. Lett.* **95** (21), 210503 (2005).
4. H. Paik and K. D. Osborn, "Reducing Quantum-Regime Dielectric Loss of Silicon Nitride for Superconducting Quantum Circuits," *Appl. Phys. Lett.* **96** (7), 072505 (2010).
5. T. Eriksson, S. Jiang, and C. Granqvist, "Dielectric function of sputter-deposited silicon dioxide and silicon nitride films in the thermal infrared," *Appl. Opt.* **24**, 745–746 (1985).
6. E. A. Taft, "Characterization of Silicon Nitride Films," *J. Electrochem. Soc.* **118**, 1341–1346 (1971).
7. E. D. Palik, *Handbook of Optical Constants of Solids*, Vol. 1 (Elsevier, 1998), pp. 771–774.
8. M. Sekimoto, H. Yoshihara, and T. Ohkubo, "Silicon Nitride Single-Layer X-Ray Mask," *J. Vac. Sci. Technol.* **21** (4), 1017–1021 (1982).
9. T. Makino, "Composition and Structure Control by Source Gas Ratio in LPCVD SiN<sub>x</sub>," *J. Electrochem. Soc.* **130** (2), 450–455 (1983).
10. Addison Engineering, 150 Nortech Parkway, San Jose, CA 95134. (Orientation <100>, Czochralski, p-type B doped, bulk resistivity < 0.005  $\Omega\cdot\text{cm}$ )
11. F. Gervais, "High-Temperature Infrared Reflectivity Spectroscopy by Scanning Interferometry" in *Electromagnetic Waves in Matter*, Part I, Vol. 8 (Infrared and Millimeter Waves), K. J. Button, eds. (Academic Press, London, 1983), pp. 284–287.
12. C. C. Kim, J. W. Garland, H. Abad, and P. M. Raccah, "Modeling the optical dielectric function of semiconductors: Extension of the critical-point parabolic-band approximation," *Phys. Rev. B* **45** (20), 11749 (1992).
13. P. Yeh, *Optical Waves in Layered Media* (Wiley, New York, 1988), pp. 102–111.
14. M. C. Biggs, "Constrained Minimization Using Recursive Quadratic Programming," in *Towards Global Optimization*, L. C. W. Dixon and G. P. Szergo, eds. (North-Holland, 1975), pp. 341–349.
15. M. J. D. Powell, "Variable Metric Methods for Constrained Optimization," in *Mathematical Programming: The State of the Art*, A. Bachem, M. Grottschel and B. Korte, eds. (Springer Verlag, 1983), pp. 288–311.
16. L. D. Landau and E. M. Lifshitz, *Electrodynamics of Continuous Media*, Vol. 8 (Pergamon Press, 1960), pp. 253–262.
17. M. Mori and T. Ooura, "Double Exponential Formulas for Fourier Type Integrals with a Divergent Integrand," in *Applicable Analysis*, Vol. 2 (World Scientific Series, 1993), pp. 301–308.
18. R. Nitsche and T. Fritz, "Determination of model-free Kramers-Kronig consistent optical constants of thin absorbing films from just one spectral measurement: Application to organic semiconductors," *Phys. Rev. B* **70** (19), 195432 (2004).
19. W. H. Press, S. A. Teukolsky, W. T. Vetterling, and B. P. Flannery, *Numerical Recipes - The Art of Scientific Computing* (Cambridge University Press, 2007), pp. 799–806.